ARCHIVES OF ACOUSTICS Vol. 51, No. 1, pp. 25–36 (2026), https://doi.org/10.24423/archacoust.2026.4290

Research Paper

Analysis on Modal Distribution and Modal Density-Based Crossover Frequency in Cabin-Sized Enclosures

Ziyu WANG[(1)], Liangfen DU[(2)], Guangzheng YU[(1)*]

[(1)] *Acoustic Laboratory, School of Physics and Optoelectronics, South China University of Technology* Guangzhou, China

[(2)] *Department of Building Environment and Energy Engineering, Hong Kong Polytechnic University* Hung Hom, Hong Kong

*Corresponding Author: scgzyu@scut.edu.cn

Received July 30, 2025; revised November 14, 2025; accepted November 24, 2025; available online January 16, 2026; version of record February 10, 2026; published issue March 27, 2026.

In the sound field simulation of cabin-sized enclosures, the Schroeder frequency (SF) is still employed to estimate the crossover frequency (CF) that determines the validity ranges of wave-based and geometrical acoustic methods. However, because cabin-sized enclosures exhibit distinct modal behaviors from typical medium- and large-scale rooms, the validity of SF in such enclosures has not been thoroughly tested. This study introduces the modal density-based crossover frequency (MDCF) to systematically evaluate the applicability of SF in cabin-sized enclosures. The MDCF employs the same dense modal criterion as SF. However, its modal parameters, are derived from the numerical eigenfrequency analysis. This contrasts with the SF formula, where these parameters are determined solely by the room volume and reverberation time. Ten models are constructed for evaluation, grouped into two volume sets: 8 m^3 (cabin-sized) and 80 m^3 (common-sized). Each set comprises five distinct geometrical shapes from rectangular models to simplified vehicle shapes. The results reveal that, for cabin-sized enclosures under low absorption boundary conditions, the MDCF is typically 70 Hz to 150 Hz lower than SF; the discrepancies decrease to 20 Hz to 50 Hz in 80 m^3 rooms. Furthermore, the MDCF varies with room shapes at a constant volume, while the SF remains nearly unchanged. These findings demonstrate that MDCF provides a more reliable CF estimation for rooms with irregular shapes, highlighting the importance of considering accurate modal parameters in the acoustic analysis of cabin-sized models.

Keywords: vehicle acoustics, room acoustic modes, crossover frequency, Schroeder frequency.

Notations

B_{HP} – half-power bandwidth,
$\widetilde{B}_{HP}$ – simplified half-power bandwidth,
$B_{HP}(f_{n,c})$ – n-th half-power bandwidth,
$\mathbf{C}$ – damping matrix,
c_0 – speed of sound,
f_{MDCF} – modal density-based crossover frequency,
f_n – n-th eigenfrequency under rigid boundary (or the real part of n-th eigenfrequency $f_{n,c}$),
$f_{n,c}$ – n-th eigenfrequency
f_{SF} – Schroeder frequency,
f_u – upper limit frequency,
k – wavenumber,
$\mathbf{K}$ – stiffness matrix,
L – total edge length,
L_x, L_y, L_z – room dimensions,
M – modal overlap degree,
$\mathbf{M}$ – mass matrix,
N_f – modal number,
$\widetilde{N}_f$ – simplified modal number,
n_x, n_y, n_z – modal orders along each axis,
p – sound pressure,
S – total surface area,
T_{60} – reverberation time,
V – volume,

Z – boundary acoustic impedance,
α – absorption coefficient,
δ – modal decay factor,
$\widetilde{\delta}$ – simplified modal decay factor,
$\delta_{n,c}$ – n-th modal decay factor,
Δf_n – eigenfrequency spacing,
$\Delta\widetilde{f}_n$ – simplified eigenfrequency spacing,
ρ – air density,
ζ – normalized boundary impedance, $\zeta = \zeta_i + j\zeta_r$.

1. Introduction

In the study of sound field simulation and analysis for cabin-sized enclosures, the crossover frequency (CF) serves as a critical threshold that defines the optimal transition between wave-based and geometrical acoustic methods (Kleiner, Tichy, 2014; Rougier, 2018; Siltanen *et al.*, 2010). Below the CF, the sound field is dominated by a limited set of discrete normal modes, where the wave-based methods such as the finite element method (FEM) can provide accurate predictions (Sakuma *et al.*, 2014). Above the CF, the modal density increases, leading to a more even distribution of sound energy; therefore, geometrical acoustic methods – ray tracing methods – provide accurate predictions with greater computational efficiency (Savioja, Svensson, 2015; Savioja, Xiang, 2019).

In practice, CF is commonly estimated by the classical Schroeder frequency (SF) formula, which has been validated mainly in the medium- and large-scale sound fields (Southern *et al.*, 2011; 2013; Summers *et al.*, 2004). Based on the statistic acoustic theory, the SF is determined by two parameters: the room volume V, which describes the modal distribution behavior, and the reverberation time T_{60}, which characterize the decay rates of all modes (Schroeder, Kuttruff, 1962; Schroeder, 1987; 1996). Both the modal distribution and the modal decay properties serve as critical parameters for the theoretical determination of CF, and SF offers a convenient indicator for estimating CF (Brinkmann *et al.*, 2019).

However, the simplifications and assumptions of modal properties in the derivation of SF impose limitations. The simplified modal distribution formula – originally derived from the distribution of oblique modes in rectangular rooms – approximates the modal distribution of enclosures with different shapes solely through their volumes V (Bolt, 1946; Morse, Uno Ingard, 1968); it not only undercounts modes but also neglects the effects of room geometry on modal distribution (Gunawan, Aditanoyo, 2018; Meissner, 2021). The reverberation time T_{60}, which characterizes the modal decay rate, is typically assumed to be a frequency-independent value – estimated either from an average absorption coefficient in analytical simulation or from the 1 kHz one-third octave band in measurements – to yield a specific SF value (Kuttruff, 2016; Nélisse, Nicolas, 1997). Such a single global parameter T_{60}, however, is insufficient to capture the decay behaviors of individual modes. Because the decay rate of each mode depends on how it interacts with the damping boundaries: modes that encounter more damping surfaces exhibit faster energy decay than those encountering fewer damping surfaces (Bastine *et al.*, 2021; Zheng *et al.*, 2021). For instance, in rectangular rooms, the oblique modes decay more rapidly than the axial and tangential modes, and similar variations are also observed in non-rectangular enclosures.

The limitations from the simplified modal parameters become more pronounced in cabin-sized enclosures. In such enclosures, the number of modes within a given frequency band is limited and their distribution is sparse (Kleiner, Tichy, 2014; Meissner, 2017). Therefore, any underestimation using a volume-based formula can lead to substantial relative errors. Moreover, the premise of reverberation time T_{60} is often invalid in cabin-sized enclosures due to the rapid interaction of sound waves with damping boundaries, which causes faster energy decay (Ferreira *et al.*, 2016; Rindel, 2015). As a result, these simplified modal parameters introduce significant errors into the modal analysis of cabin-sized enclosures. Despite these limitations, the SF remains a reference for estimating the CF in several vehicle acoustics studies (Aretz, Vorländer, 2014a; 2014b; Granier *et al.*, 1996; Pinardi *et al.*, 2021). Hence, it is necessary to reassess the validity of using SF to estimate CF, as its applicability in this context is insufficiently established.

To address these issues, this study analyzes the modal characteristics of cabin-sized enclosures, and proposes the modal density-based crossover frequency (MDCF) for CF estimation using accurate modal parameters. Ten models – comprising two volume sets (8 m^3 and 80 m^3) and five distinct geometries per set – are simulated via the FEM to obtain accurate eigenfrequencies and modal parameters. By comparing the numerically derived modal

spacing and bandwidth with analytical solutions, we quantify the discrepancies between MDCF with SF, and elucidate the mechanisms underlying these differences in cabin-sized enclosures.

The paper is organized as follows: Sec. 2 introduces the research models, including the model shapes, boundary conditions, and numerical simulation setup; Sec. 3 reviews the analytical formulas and numerical simulations of modal parameters, details the derivation process of the SF and MDCF, and presents the relations between them; Sec. 4 compares the results between analytical (SF-based) and numerical (MDCF-based) modal parameters across different geometries and boundary conditions, and further compares the MDCF and SF. Finally, Sec. 5 concludes with the main findings and academic contributions of MDCF in vehicle acoustics studies.

2. Research models

The research models comprise two sets of proportionally scaled models with a volume ratio of 1:10, the small-scale set has a volume of $8\,\mathrm{m}^3$, representing vehicle cabins, while the large-scale set has a volume of $80\,\mathrm{m}^3$, representing ordinary meeting rooms. Each volume set contains five geometrical configurations: three rectangular rooms with dimension ratios ($L_x : L_y : L_z$) as follows – model A (1.00 : 3.00 : 4.00), model B (1.00 : 1.50 : 2.50), and model C (1.00 : 1.20 : 1.45) (Rindel, 2021), and two chamfered models: model D and model E, created by applying diagonal cuts to model B (similar dimensions to actual cabins). Figure 1 provides the exact dimensions and geometries for the five small-scale models ($8\,\mathrm{m}^3$).

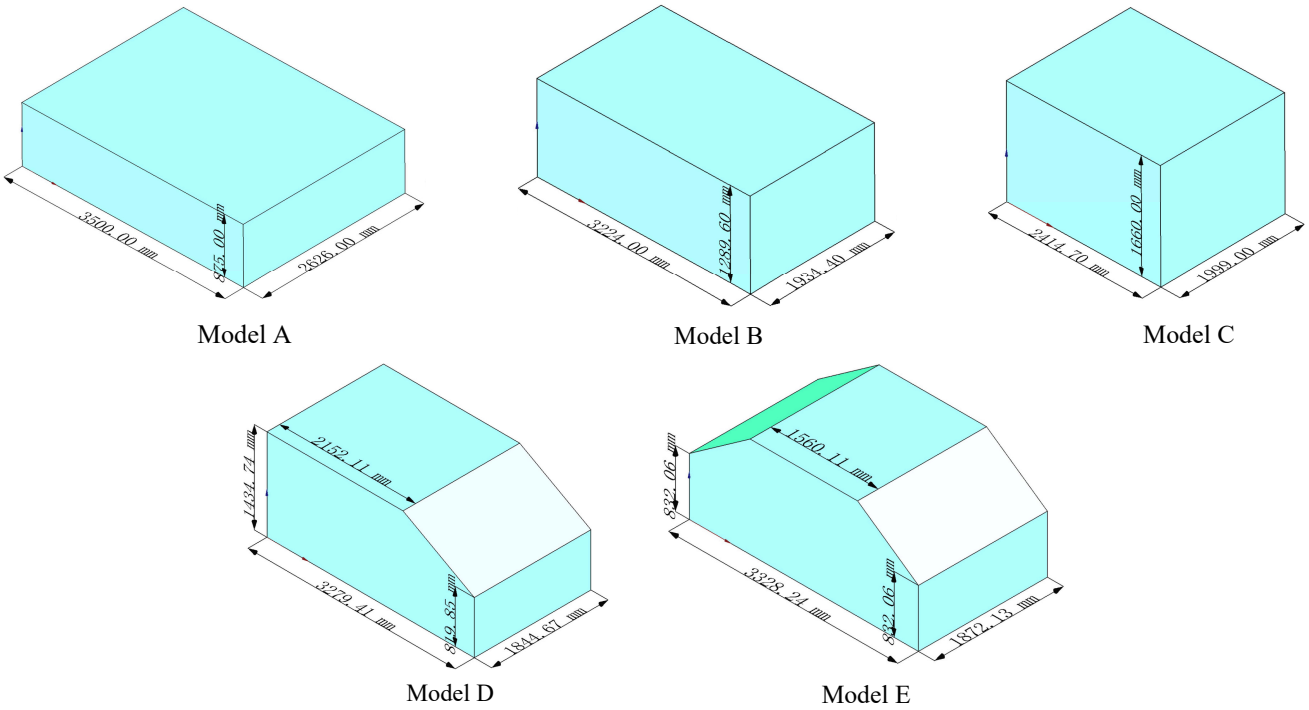

Fig. 1. Dimensions and geometries of five small-scale models. Rectangular models: model A (1.00 : 3.00 : 4.00), model B (1.00 : 1.50 : 2.50), model C (1.00 : 1.20 : 1.45). Non-rectangular models: model D (one oblique plane), model E (two oblique planes). Dimensions are in millimeters [mm].

All interior surfaces are modeled as isotropic and homogeneous boundaries, with a uniform absorption coefficient a ranging from 0.05 to 0.30. Boundary losses are implemented by locally reacting boundaries with Robin boundary conditions (Zheng *et al.*, 2021).

Acoustic eigenmodes are obtained by solving the linearized Helmholtz equation under rigid or damping boundary conditions via the FEM, the calculation process is detailed in the next section. The computational mesh element size is set to $h \leq \frac{\lambda_{\min}}{5}$, where $\lambda_{\min} = 0.0686\,\mathrm{m}$ corresponds to the wavelength at 1 kHz, ensuring a minimum of five elements per wavelength for simulation accuracy.

3. Theory and methods

Modal distribution and modal decay are fundamental properties of normal modes. This section first outlines the theoretical framework of modal theory and the analytical formulas for modal parameters in rectangular rooms, followed by the derivation of the SF. Based on this framework, the corresponding parameters for non-rectangular rooms are obtained through the numerical eigenfrequency analysis. Subsequently, the MDCF is introduced as an alternative estimation method for estimating the CF, and its differences from the SF formula are compared and discussed.

3.1. Analytical solution of modal parameters and derivation of the Schroeder frequency

For a rectangular room with rigid boundaries, the eigenfrequency formula is given by (Kuttruff, 2016):

$$f_n = \frac{c_0}{2}\sqrt{\left(\frac{n_x}{L_x}\right)^2 + \left(\frac{n_y}{L_y}\right)^2 + \left(\frac{n_z}{L_z}\right)^2}, \tag{1}$$

where c_0 is the speed of sound in air, L_x, L_y, L_z are the room dimensions, and n_x, n_y, n_z are non-negative integers representing the modal orders along each axis. Modes are classified according to their propagation direction: oblique modes (none of the n_x, n_y, n_z are zero, representing 3D volume propagation), tangential modes (one of the n_x, n_y, n_z is zero, indicating 2D surface propagation), and axial modes (two of the n_x, n_y, n_z are zero, corresponding to 1D axial propagation).

The modal number below an upper frequency f_u in rectangular rooms is given by (Maa, 1939):

$$N_f(f_u) = \frac{4\pi}{3}V\left(\frac{f_u}{c_0}\right)^3 + \frac{\pi}{4}S\left(\frac{f_u}{c_0}\right)^2 + \frac{L}{8}\frac{f_u}{c_0}, \tag{2}$$

where V, S, and L represent the room volume, total surface area, and sum of the room edge lengths, respectively. Since the first volume-governed term dominates at high frequencies, Eq. (2) is commonly simplified as (Weyl, 1911):

$$\widetilde{N}_f(f_u) = \frac{4\pi}{3}V\left(\frac{f_u}{c_0}\right)^3. \tag{3}$$

The eigenfrequency spacing, defined as the difference between consecutive eigenfrequencies, can also be expressed as the number of modes within per unit frequency range. Based on Eq. (3), the average eigenfrequency spacing is expressed as

$$\Delta\widetilde{f}_n = \left(\frac{\mathrm{d}\widetilde{N}_f(f_u)}{\mathrm{d}f_u}\right)^{-1} = \frac{c_0^3}{4\pi V f_u^2}. \tag{4}$$

Under non-rigid boundary conditions, modal energy decays over time. The decay rate is typically quantified by the decay factor δ, following the relation of $E(t) = E_0 e^{-2\delta t}$. The decay factor can be derived from the time required for the sound level decreases by 60 dB, known as T_{60}. Thus, the decay factor is given by (Kuttruff, 2016):

$$\widetilde{\delta} = \frac{3\ln(10)}{T_{60}}. \tag{5}$$

In the frequency region, the half-power bandwidth – defined as the frequency range where energy decays from peak to half-peak – is related to the decay factor by (Kuttruff, 2016):

$$B_{HP} = \frac{\delta}{\pi}. \tag{6}$$

By substituting the Eq. (5) into Eq. (6), the half-power bandwidth can be expressed as

$$\widetilde{B}_{HP} = \frac{3\ln(10)}{\pi \cdot T_{60}}. \tag{7}$$

The modal overlap degree is defined as the ratio of half-power bandwidth and eigenfrequency spacing, can be calculated as (Dance, Van Buuren, 2013):

$$M = \frac{B_{HP}}{\Delta f_n}. \tag{8}$$

According to Schroeder's study, when the modal overlap degree reaches or exceeds 3 – that is, when the eigenfrequencies spacing is less than one-third of the bandwidth – it represents the dense modal distribution (Schroeder, 1996). This criterion can be reformulated as the condition where the half-power bandwidth equals three times of eigenfrequency spacing, expressed as

$$B_{HP} = 3 \times \Delta f_n. \tag{9}$$

By substituting the expressions for eigenfrequency spacing from Eq. (4) and the half-power bandwidth from Eq. (7), the Schroeder frequency is expressed as

$$f_{\mathrm{SF}} = 2065.8 \sqrt{\frac{T_{60}}{V}} \approx 2000 \sqrt{\frac{T_{60}}{V}}. \tag{10}$$

Therefore, the SF provides a general formula, based on the room volume V and decay parameter T_{60}, to estimate the CF, which marks the transition from the discrete to dense modal distribution.

3.2. Numerical modal analysis and the definition of modal density-based crossover frequency

However, in a non-rectangular enclosure with complex boundary conditions, the analytical eigenfrequency formula – Eq. (1) – is no longer applicable. In practice, the FEM and other numerical simulation methods can provide a viable and efficient way to predict the eigenfrequency, as obtaining exact eigenvalues by measurements is often impractical. The FEM solves for the eigenfunctions by discretizing the continuous governing equations (Sakuma *et al.*, 2014). All models in this study are analyzed using the FEM to ensure comparability.

The governing equation (the Helmholtz equation) in the acoustic eigenmode analysis takes the form:

$$\nabla^2 p + k^2 p = 0, \tag{11}$$

where $k = \frac{\omega}{c_0}$ is the wavenumber. Through the Galerkin weighted residual method, the continuous Eq. (11) is discretized into a generalized matrix eigenproblem, with eigenfunctions Φ and corresponding eigenvalues k:

$$\left[\mathbf{K} - k^2 \mathbf{M}\right] \Phi = 0, \tag{12}$$

where $K_{ij} = \int_{\Omega} \nabla D_i \cdot \nabla D_j \, \mathrm{d}\Omega$ is the element of the stiffness matrix $\mathbf{K}$, and $M_{ij} = \int_{\Omega} D_i D_j \, \mathrm{d}\Omega$ is an element of the mass matrix $\mathbf{M}$; D_i and D_j represent shape functions for nodes i and j, and Ω is the computational volume domain.

Based on the numerical eigenfrequency solutions, the eigenfrequency spacing is calculated as the difference between consecutive eigenfrequencies. Compared to Eq. (4), this approach is fundamental and yields randomly fluctuating results rather than an averaged trend:

$$\Delta f_n = f_n - f_{n-1}. \tag{13}$$

Under damping boundary conditions with a specific acoustic impedance Z, the governing equation is modified as

$$\left(\mathbf{K} - k^2 \mathbf{M} + \mathbf{C}\right) \Phi = 0, \tag{14}$$

where $C_{ij} = \frac{i\omega\rho}{Z} \int_{S} D_i D_j \, \mathrm{d}S$ is an element of the damping matrix $\mathbf{C}$, ρ is the ambient air density, and S is the computational surface domain. Consequently, the n-th eigenfrequency is expressed as

$$f_{n,c} = f_n - i\frac{\delta_{n,c}}{2\pi}, \tag{15}$$

where the imaginary part represents the mode-specific decay factor $\delta_{n,c}$, which varies with the modal propagation direction and boundary conditions. Substituting $\delta_{n,c}$ into Eq. (6) yields the mode-specific half-power bandwidth:

$$B_{HP}\left(f_{n,c}\right) = \frac{\delta_{n,c}}{\pi}. \tag{16}$$

Applying the same criterion: 'three modes within a half-power bandwidth B_{HP},' the MDCF is defined from the numerical eigenfrequency solutions. As illustrated in Fig. 2, for each eigenfrequency $f_{n,c}^{(i)}$, the number of modes $N_f^{(i)}$ within its corresponding half-power bandwidth $B_{HP}(f_{n,c}^{(i)})$ is counted. The MDCF is identified as the lowest eigenfrequency for which the half-power bandwidth contains three or more modes, and all subsequent frequencies also satisfy this condition. The half-power bandwidth and its center frequency correspond to the imaginary and real parts of the complex eigenfrequency in Eq. (15).

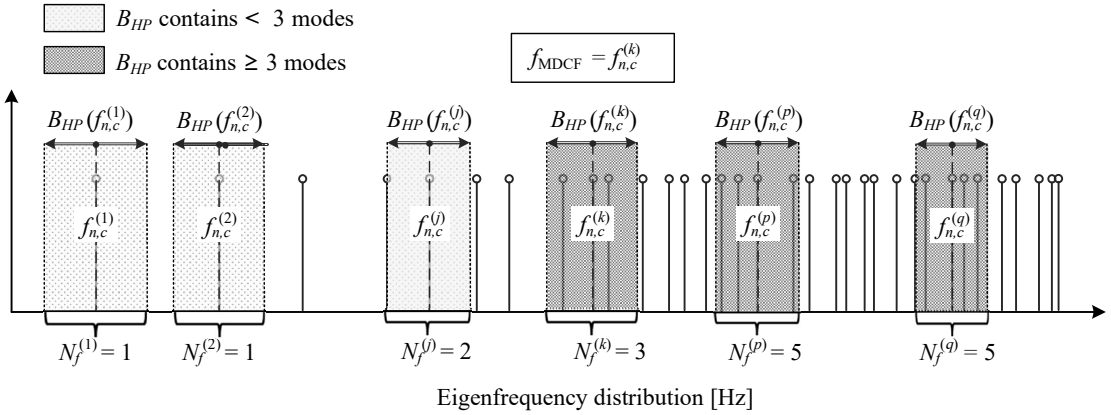

Fig. 2. Definition of modal density-based crossover frequency: the MDCF is the lowest eigenfrequency whose half-power bandwidth contains three or more modes, with all subsequent frequencies also meeting this criterion.

As shown in Fig. 2, light gray blocks represent bands that do not satisfy the dense modal criterion, such as $B_{HP}\left(f_{n,c}^{(1)}\right)$; while dark gray blocks satisfy this criterion. Since the $B_{HP}\left(f_{n,c}^{(k)}\right)$ centered at the eigenfrequency $f_{n,c}^{(k)}$ contains three modes of $N_f^{(k)}$, and all subsequent frequency bands also satisfy this condition, it follows that $f_{\mathrm{MDCF}} = f_{n,c}^{(k)}$.

3.3. Comparison of Schroeder frequency and modal density-based crossover frequency

Both of SF and MDCF employ the 'three mode within a B_{HP}' criterion, but they differ in the employed parameters and derivation process. Table 1 summarizes the modal parameters used in the derivation of SF and MDCF.

Table 1. Modal parameters employed in derivation process of SF and MDCF.

Parameter	Schroeder frequency	Modal density-based crossover frequency
Eigenfrequency spacing	$\Delta\widetilde{f}_n = \frac{c_0^3}{4\pi V f_u^2}$, simplified formulas (rectangular shape)	$\Delta f_n = f_n - f_{n-1}$, numerical results (any geometrical shapes)
Half-power bandwidth	$\widetilde{B}_{HP} = \frac{3\ln(10)}{\pi \cdot T_{60}}$, with global decay T_{60}	$B_{HP}\left(f_{n,c}\right) = \frac{\delta_{n,c}}{\pi}$, mode-dependent

4. Results

The modal parameters obtained from numerical simulations and analytical formulas are compared in the following section.

4.1. Eigenmode distributions under rigid walls

Figure 3 presents the comparison of eigenfrequency spacing under the rigid boundary condition. The numerical results Δf_n from Eq. (13) in 8 m^3 and 80 m^3 rooms are shown as green- and blue-marked lines, respectively; while analytical results $\Delta \widetilde{f}_n$ from Eq. (4) are presented by black dashed and dotted lines. The gray shaded areas indicate the discrepancies between the two methods.

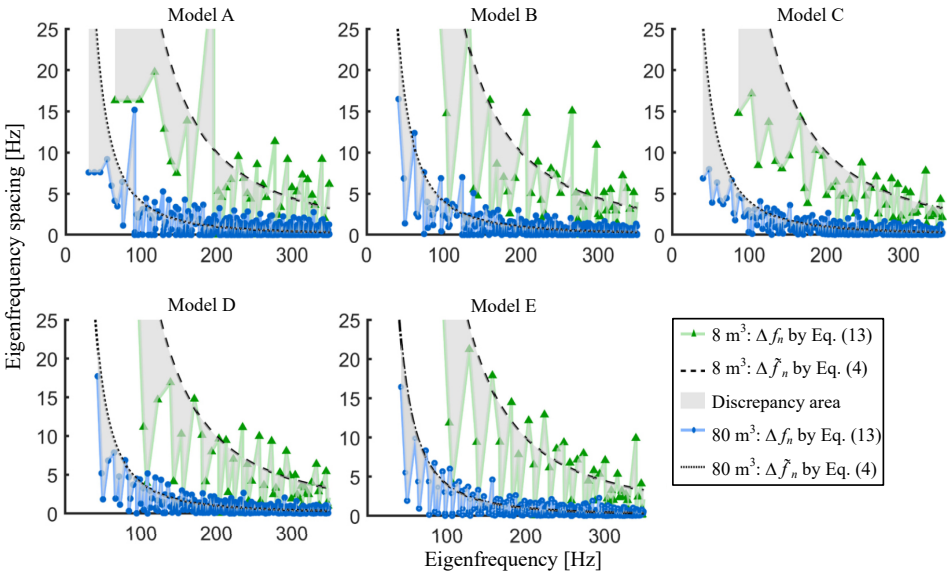

Fig. 3. Eigenfrequency spacing from numerical results Δf_n from Eq. (13) and analytical results $\Delta \widetilde{f}_n$ from Eq. (4) in 8 m^3 rooms (green-marked lines, black-dashed lines) and 80 m^3 rooms (blue-marked lines, black-dotted lines). Gray regions denote discrepancies between them.

Overall, discrepancies are observed across all models, and are more pronounced in small-scale rooms (8 m^3). In the low-frequency range, the eigenfrequency spacings obtained from the analytical results are higher than that from the numerical results, and gradually consistent. For example, below 200 Hz, the average difference between the two methods range from 10 Hz to 20 Hz in 8 m^3 rooms; and from 3 Hz to 10 Hz in 80 m^3 rooms.

Regarding the shape-dependent discrepancies in 8 m^3 rooms, model A exhibits the largest deviation, with differences up to 20 Hz. Models B and E also show substantial discrepancies, with maximum deviations of 10 Hz to 15 Hz. Models C and D display smaller differences, with deviations around 10 Hz. These results indicate that the analytical method becomes less accurate in small-scale enclosures, ultimately affecting the analysis of modal overlap and crossover frequency.

4.2. Half-power bandwidth under damping boundaries

Figure 4 compares the half-power bandwidths under a uniform absorption boundary condition (α = 0.20). The numerical bandwidths $B_{HP}(f_{n,c})$ from Eq. (16) for 8 m^3 and 80 m^3 rooms are presented by green- and blue-marked lines, respectively; and analytical results $\widetilde{B}_{HP}$ from Eq. (7) are shown as black dashed and dotted lines. The gray areas quantify the deviations between the two methods.

Across all models, the bandwidths obtained numerically are consistently higher than those from the analytical formula, and this discrepancy is more pronounced in 8 m^3 rooms. For instance, in 8 m^3 rooms, deviations exceed 10 Hz at certain eigenfrequencies; whereas the discrepancy is narrower in 80 m^3 rooms. Moreover, the numerical results exhibit frequency-dependent variations: at low frequencies, they show a scattered distribution due to varying modal damping; whereas at high frequencies, they stabilize at a higher value owing to the dominance of oblique modes. In contrast, the analytical results remain constant across the frequency range.

As for the shape-dependent discrepancies in 8 m^3 rooms, model C has the largest deviation (nearly 15 Hz), followed by models B and E (up to 10 Hz), and model D (slightly less than 10 Hz). Model A exhibits the smallest

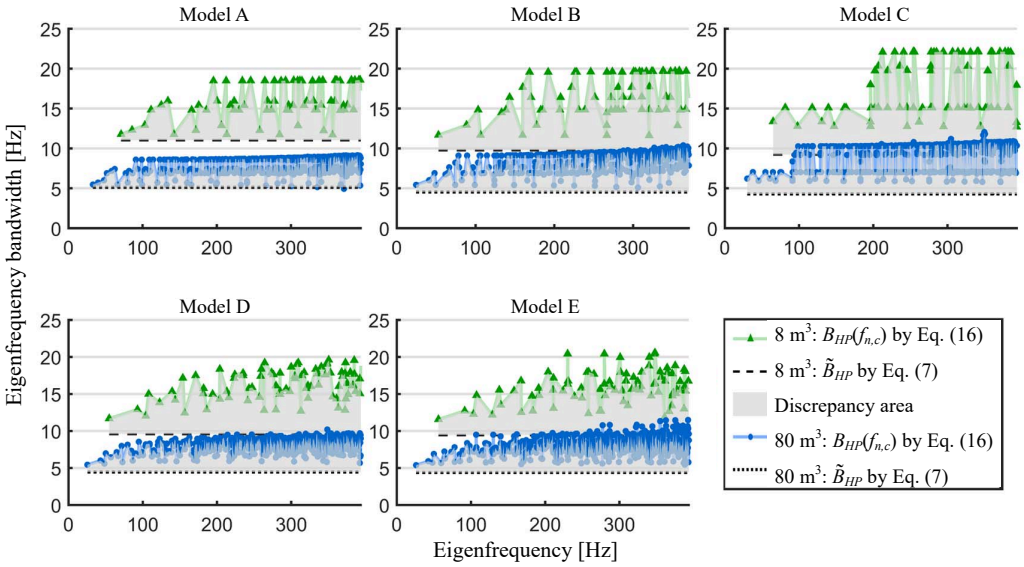

Fig. 4. Half-power bandwidth of numerical results $B_{HP}(f_{n,c})$ from Eq. (16) and analytical results $\widetilde{B}_{HP}$ from Eq. (7) in 8 m^3 rooms (green-marked lines, black-dashed lines), and 80 m^3 rooms (blue-marked lines, black-dotted lines). The boundary absorption coefficient is 0.20, and T_{60} in analytical $\widetilde{B}_{HP}$ is obtained by Eyring T_{60} formula. Gray regions denote discrepancies between them.

discrepancy. These results demonstrate that the analytical formula underestimates the modal damping, and that the discrepancies between numerical and analytical results among different model shapes are more pronounced in small-scale enclosures.

4.3. Modal overlap degree

The ratio of the half-power bandwidth to eigenfrequency spacing is the modal overlap degree, which determines the final crossover frequency. Figure 5 compares the modal overlap degree under the boundary condition of a uniform absorption $\alpha = 0.20$. Green and blue lines represent $B_{HP}(f_{n,c})/\Delta f_n$ obtained by numerical results for 8 m^3 and 80 m^3 rooms, respectively; while black-dashed and dotted lines show $\widetilde{B}_{HP}/\Delta\widetilde{f}_n$ obtained by the analytical formula. Gray areas indicate where a modal overlap degree reach or exceed three. The vertical solid and dashed lines indicate the MDCF and SF for 8 m^3 rooms (green) and 80 m^3 rooms (blue). Above the MDCF and SF, the modal overlap degree exceeds three.

This analysis is critical for determining the MDCF and SF. Overall, the modal overlap degree from numerical results is consistently higher than that from analytical results under the current boundary condition; correspondingly, MDCF is generally lower than the SF in all models except model C, where a sudden drop in the modal bandwidth containing fewer than three modes results in a higher MDCF.

Notably, the difference between MDCF and SF is more pronounced in 8 m^3 rooms. For example, model D exhibits the largest gap, around 140 Hz (MDCF ≈ 220 Hz and SF ≈ 360 Hz), followed by model E at approximate 100 Hz, model B is around 60 Hz, and model A is around 40 Hz. In contrast, 80 m^3 rooms show narrower gaps between MDCF and SF, around 15 Hz to 40 Hz. Based on this methodology, results for other boundary conditions could be derived similarly and are presented in the next section.

4.4. Modal density-based crossover frequency

Based on the foregoing analysis, the MDCF can be determined. Figure 6 compares MDCF with SF in 8 m^3 and 80 m^3 rooms for the boundary absorption coefficients in the range of [0.05, 0.30]. The MDCF is represented by marked lines and SF is represented by dashed lines.

The results show that the MDCF is generally lower than the SF in most cases. Notably, larger discrepancies are observed in 8 m^3 rooms than 80 m^3 rooms. For instance, at $\alpha = 0.20$, the differences of MDCF and SF exhibit

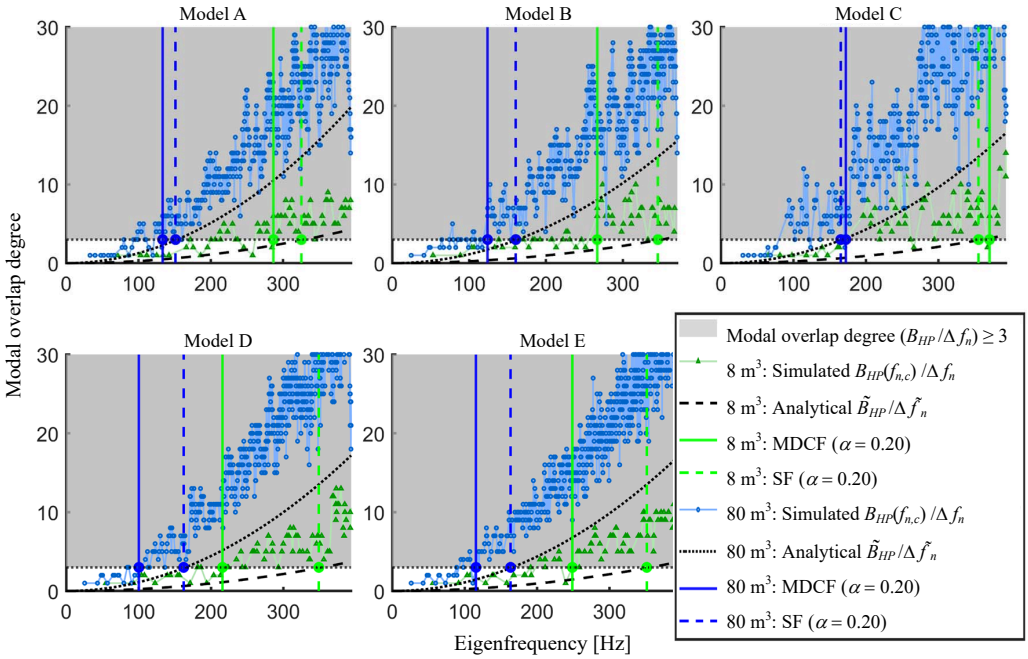

Fig. 5. Modal overlap degree of numerical modal parameters $(B_{HP}(f_{n,c})/\Delta f_n)$ and analytical modal parameters $(\widetilde{B}_{HP}/\Delta\widetilde{f}_n)$ in 8 m^3 rooms (green-marked lines, black-dashed lines) and 80 m^3 rooms (blue-marked lines, black-dotted lines). The boundary absorption coefficient is 0.20. The vertical lines represent the MDCF (solid lines) and SF (dashed lines) in 8 m^3 rooms (green) and 80 m^3 rooms (blue), indicating the frequency beyond which the bandwidth contains more than three modes.

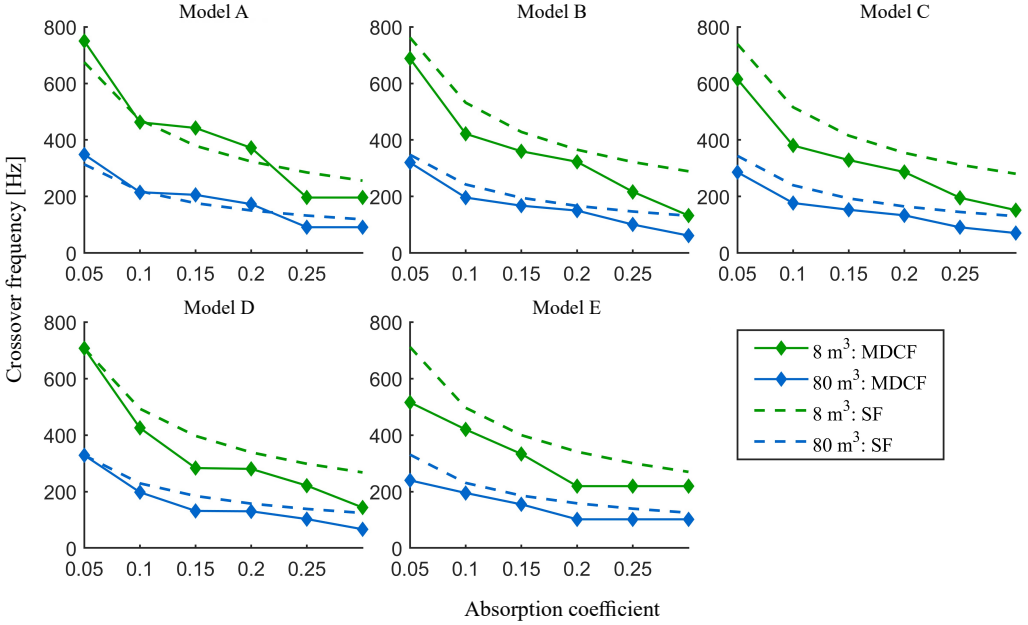

Fig. 6. MDCF and SF in 8 m^3 (green-solid and dashed lines) and 80 m^3 (blue-solid and dashed lines) rooms, when boundary absorption coefficient is from 0.05 to 0.30.

an average of 55 Hz and the peak of 145 Hz in 8 m^3 rooms, whereas in 80 m^3 rooms, the average gap is 25 Hz, and the peak gap is 50 Hz. As analyzed above, discrepancies in the eigenfrequency spacing and half-power bandwidth between numerical and analytical results lead to differences between the MDCF and the SF. These include: the MDCF accounts for actual modal distribution, considering all simulated eigenmodes, and the SF relies on volume-related eigenmodes that overestimate eigenfrequency spacing, particularly in small-scale rooms; and the numerical B_{HP} is consistently wider than analytical predictions, with this discrepancy amplified in smaller enclosures. These

findings explain the mechanisms underlying the discrepancies between the SF and the MDCF when estimating the CF, and quantitatively specify these differences.

5. Conclusion

This study investigates modal characteristics of cabin-sized enclosures by analyzing two key parameters that determine the CF – modal distribution and modal decay – using both numerical simulations and analytical formulations. The MDCF, derived from numerical simulations, is proposed and compared with the SF. Based on ten models with two volumes and five different geometrical shapes, the results show that the MDCF varies with room shapes at a constant volume. Furthermore, the MDCF is lower than SF approximately 70 Hz to 150 Hz in cabin-sized rooms; while the differences decrease from 20 Hz to 50 Hz in larger rooms. Consequently, MDCF provides a more reliable CF estimation for irregularly shaped rooms, and highlights the necessity of incorporating accurate modal parameters in the modal analysis of cabin-sized enclosures. Additionally, the difference in modal decay rates across modal types is analyzed, providing theoretical insights relevant to low-frequency equalization. Future work should include experimental validation to deepen the understanding of modal properties in cabin-sized enclosures.

Fundings

This work was supported by the National Natural Science Foundation of China (grant no. 12474465) and the Natural Science Foundation of Guangdong Province (grant no. 2024A1515011446).

Conflict of interest

The authors declare that they have no known competing financial interests or personal relationships that could have appeared to influence the work reported in this paper.

Authors' contributions

Ziyu Wang conceptualized the study, performed the data analysis and interpretation, wrote the original draft. Liangfen Du contributed to data interpretation and review the original draft. Guangzheng Yu contributed to conceptualize the study and review the original draft. All authors reviewed and approved the final manuscript.

Data availability

The data that support the findings of this study are available within the article.

References

1. Aretz M., Vorländer M. (2014a), Combined wave and ray based room acoustic simulations of audio systems in car passenger compartments, Part I: Boundary and source data, *Applied Acoustics*, **76**: 82–99, https://doi.org/10.1016/j.apacoust.2013.07.021.
2. Aretz M., Vorländer M. (2014b), Combined wave and ray based room acoustic simulations of audio systems in car passenger compartments, Part II: Comparison of simulations and measurements, *Applied Acoustics*, **76**: 52–65, https://doi.org/10.1016/j.apacoust.2013.07.020.
3. Bastine A., Abhayapala T.D., Zhang J.A. (2021), Power response and modal decay estimation of room reflections from spherical microphone array measurements using Eigenbeam spatial correlation model, *Applied Sciences*, **11**(16): 7688, https://doi.org/10.3390/app11167688.
4. Bolt R.H. (1946), Note on normal frequency statistics for rectangular rooms, *The Journal of the Acoustical Society of America*, **18**(1): 130–133, https://doi.org/10.1121/1.1916349.

5. Brinkmann F., Aspöck L., Ackermann D., Lepa S., Vorländer M., Weinzierl S. (2019), A round robin on room acoustical simulation and auralization, *The Journal of the Acoustical Society of America*, **145**(4): 2746–2760, https://doi.org/10.1121/1.5096178.
6. Dance S.M., Van Buuren G. (2013), Effects of damping on the low-frequency acoustics of listening rooms based on an analytical model, *Journal of Sound and Vibration*, **332**(25): 6891–6904, https://doi.org/10.1016/j.jsv.2013.07.011.
7. Ferreira T.S., Magalhães P.A., Moura F.L., Ferreira T.S. (2016), The effect of the cavity damping on vehicular evaluation using the finite element method, *Archives of Acoustics*, **41**(1): 87–97, https://doi.org/10.1515/aoa-2016-0009.
8. Granier E., Kleiner M., Dalenbäck B.-I., Svensson P. (1996), Experimental auralization of car audio installations, *Journal of the Audio Engineering Society*, **44**(10): 835–849.
9. Gunawan H., Aditanoyo T. (2018), Study of the effect of splaying wall to modify acoustic modes distribution in small room, *Journal of Physics: Conference Series*, **1075**(1): 012049, https://doi.org/10.1088/1742-6596/1075/1/012049.
10. Kleiner M., Tichy J. (2014), *Acoustics of Small Rooms*, CRC Press, https://doi.org/10.1201/b16866.
11. Kuttruff H. (2016), *Room Acoustics*, 6th ed., CRC Press, https://doi.org/10.1201/9781315372150.
12. Maa D. (1939), Distribution of eigentones in a rectangular chamber at low frequency range, *The Journal of the Acoustical Society of America*, **10**(3): 235–238, https://doi.org/10.1121/1.1915981.
13. Meissner M. (2017), Acoustics of small rectangular rooms: Analytical and numerical determination of reverberation parameters, *Applied Acoustics*, **120**: 111–119, https://doi.org/10.1016/j.apacoust.2017.01.020.
14. Meissner M. (2021), Application of modal expansion method for sound prediction in enclosed spaces subjected to boundary excitation, *Journal of Sound and Vibration*, **500**: 116041, https://doi.org/10.1016/j.jsv.2021.116041.
15. Morse P.M., Uno Ingard U. (1968), *Theoretical Acoustics*, Princeton University Press, Princeton, New Jersey.
16. Nélisse H., Nicolas J. (1997), Characterization of a diffuse field in a reverberant room, *The Journal of the Acoustical Society of America*, **101**(6): 3517–3524, https://doi.org/10.1121/1.418313.
17. Pinardi D., Riabova K., Binelli M., Farina A., Park J.-S. (2021), Geometrical acoustics simulations for ambisonics auralization of a car sound system at high frequency, [in:] *2021 Immersive and 3D Audio: from Architecture to Automotive (I3DA)*, https://doi.org/10.1109/I3DA48870.2021.9610977.
18. Rindel J.H. (2015), Modal energy analysis of nearly rectangular rooms at low frequencies, *Acta Acustica United With Acustica*, **101**(6): 1211–1221, https://doi.org/10.3813/aaa.918914.
19. Rindel J.H. (2021), Preferred dimension ratios of small rectangular rooms, *JASA Express Letters*, **1**(2): 021601, https://doi.org/10.1121/10.0003450.
20. Rougier C. (2018), *Influence of crossover frequency on a hybrid acoustic model for room impulse response synthesis*, M.Sc. Thesis, https://api.semanticscholar.org/CorpusID:115525011.
21. Sakuma T., Sakamoto S., Otsuru T. (2014), *Computational Simulation in Architectural and Environmental Acoustics: Methods and Applications of Wave-Based Computation*, Springer, Tokyo.
22. Savioja L., Svensson U.P. (2015), Overview of geometrical room acoustic modeling techniques, *The Journal of the Acoustical Society of America*, **138**(2): 708–730, https://doi.org/10.1121/1.4926438.
23. Savioja L., Xiang N. (2019), Introduction to the special issue on room acoustic modeling and auralization, *The Journal of the Acoustical Society of America*, **145**(4): 2597–2600, https://doi.org/10.1121/1.5099017.
24. Schroeder M.R. (1987), Statistical parameters of the frequency response curves of large rooms, *Journal of the Audio Engineering Society*, **35**(5): 299–306.
25. Schroeder M.R. (1996), The "Schroeder frequency" revisited, *The Journal of the Acoustical Society of America*, **99**(5): 3240–3241, https://doi.org/10.1121/1.414868.
26. Schroeder M.R., Kuttruff K.H. (1962), On frequency response curves in rooms. Comparison of experimental, theoretical, and Monte Carlo results for the average frequency spacing between maxima, *The Journal of the Acoustical Society of America*, **34**(1): 76–80, https://doi.org/10.1121/1.1909022.
27. Siltanen S., Lokki T., Savioja L. (2010), Rays or waves? Understanding the strengths and weaknesses of computational room acoustics modeling techniques, [in:] *Proceedings of the International Symposium on Room Acoustics, ISRA 2010*.

28. Southern A., Siltanen S., Murphy D.T., Savioja L. (2013), Room impulse response synthesis and validation using a hybrid acoustic model, *IEEE Transactions on Audio, Speech, and Language Processing*, **21**(9): 1940–1952, https://doi.org/10.1109/TASL.2013.2263139.

29. Southern A., Siltanen S., Savioja L. (2011), Spatial room impulse responses with a hybrid modelling method, [in:] *Audio Engineering Society 130th Convention*.

30. Summers J.E., Takahashi K., Shimizu Y., Yamakawa T. (2004), Assessing the accuracy of auralizations computed using a hybrid geometrical-acoustics and wave-acoustics method, *The Journal of the Acoustical Society of America*, **115**(5_Supplement): 2514–2515, https://doi.org/10.1121/1.4809339.

31. Weyl H. (1911), On the asymptotic distribution of eigenvalues [in German], *Nachrichten von der Gesellschaft der Wissenschaften zu Göttingen, Mathematisch-Physikalische Klasse*, **1911**: 110–117, http://eudml.org/doc/58792.

32. Zheng C., Zhao W., Gao H., Du L., Zhang Y., Bi C. (2021), Sensitivity analysis of acoustic eigenfrequencies by using a boundary element method, *The Journal of the Acoustical Society of America*, **149**(3): 2027–2039, https://doi.org/10.1121/10.0003622.